BATTERY HEALTH-CONSCIOUS POWER MANAGEMENT FOR PLUG-IN HYBRID ELECTRIC VEHICLES VIA STOCHASTIC CONTROL

Scott J. Moura[1,2] **Jeffrey L. Stein**[1] **Hosam K. Fathy**[2*]
[1]Automated Modeling Laboratory
[2]Control Optimization Laboratory
Department of Mechanical Engineering
University of Michigan
Ann Arbor, Michigan 48109-2125
Email: {sjmoura,stein,hfathy}@umich.edu

ABSTRACT

This paper investigates power management algorithms that optimally manage lithium-ion battery pack health, in terms of anode-side film growth, for plug-in hybrid electric vehicles (PHEVs). Specifically, we integrate a reduced electrochemical model of solid electrolyte interface (SEI) film formation into a stochastic dynamic programming formulation of the PHEV power management problem. This makes it possible to optimally trade off energy consumption cost versus battery health. A careful analysis of the resulting Pareto-optimal set of power management solutions provides two important insights into the tradeoffs between battery health and energy consumption cost in PHEVs. First, optimal power management solutions that minimize energy consumption cost tend to ration battery charge, while the solutions that minimize battery health degradation tend to deplete charge aggressively. Second, solutions that balance the needs for minimum energy cost and maximum battery health tend to aggressively deplete battery charge at high states of charge (SOCs), then blend engine and battery power at lower SOCs. These results provide insight into the fundamental tradeoffs between battery health and energy cost in PHEV power management.

1 INTRODUCTION

This paper investigates supervisory control algorithms that manage the tradeoff between battery pack health and energy consumption cost in plug-in hybrid electric vehicles (PHEVs). This study leverages both stochastic control theory and reduced electrochemical battery models to achieve its goal. Such health-conscious power management algorithms have the potential to increase the useful life and long-term energy capacity of battery packs. This is critically important for large-scale battery energy storage systems - ranging from PHEVs to stationary grid-scale storage - where replacement cost and cycle life are inhibiting factors. This paper's overall goal is therefore to design power management algorithms that manage battery health degradation, in the specific context of PHEVs, in some optimal sense. We pursue this goal specifically for a power-split hybrid configuration with a battery pack consisting of lithium-ion cells. Managing degradation is particularly challenging because the associated mechanisms are typically simulated using computationally intensive electrochemistry-based models that may not be directly conducive to control design. This fact is underscored in the context of the present work, which leverages dynamic programming techniques and the associated "curse of dimensionality". Moreover, PHEV power management is, by itself, a non-trivial problem that requires the solution of an optimal control problem with multiple inputs, stochastic dynamics, state and control constraints. Therefore we extend our previous research on PHEV power management [1] and lithium-ion battery health degradation simulation and model reduction [2] to solve the present problem. The resulting control algorithms tradeoff energy consumption cost with battery life by combining, for the first time, dynamic PHEV models, stochastic drive cycle models, and reduced electrochemical battery degradation models.

Three general categories of research provide the foundation for battery-health conscious hybrid vehicle power management. First, there exists a large body of literature on modeling degradation in lithium-ion batteries, including phenomena

*Address all correspondence to this author.

such as solid electrolyte interface (SEI) film formation, carbon dissolution, electrolyte degradation, and electrode structural distortion. An excellent review by Aurbach surveys these various mechanisms in depth [3]. We leverage a model particularly well-suited for model reduction and control applications that accounts for lithium diffusion dynamics, intercalation kinetics, and electrochemical potentials developed by Doyle, Fuller, and Newman [4, 5]. Ramadass *et al.* [6] added a degradation component to this model by including an irreversible solvent reduction reaction at the anode-side solid/electrolyte interface that generates a resistive film which consumes cyclable lithium. This mechanism has been identified as one of the chief contributors to capacity and power fade, whose effect is also representative of other mechanisms. The second relevant body of research considers the general HEV power management problem. A broad spectrum of optimal control techniques have been developed to solve the power management problem. Examples include equivalent consumption minimization strategy [7], model predictive control [8], deterministic dynamic programming [9, 10], and stochastic dynamic programming [1, 11]. These strategies are optimized for objectives such as fuel consumption [7–11], emissions [12], drivability [13], and/or combined fuel/electricity consumption [1]. Our focus is to apply stochastic dynamic programming with the objective of minimizing anode-side film growth, using a reduced form version of a degrading electrochemical battery model. Several more recent studies have considered the HEV power management problem for extending battery life. These studies focus on depth of discharge control [14,15], power electronics management [16], and temperature management [17]. To date, however, no studies have applied models that explicitly account for specific electrochemical degradation mechanisms in the context of an optimal control framework, to the authors' knowledge.

The main goal of this paper is to extend and connect the above research on battery health management and PHEV power management by adding three important and original contributions. First, we directly model daily vehicle trip lengths using a Markov chain with a terminal state, identified from real-world survey data. Second, we formulate a multi-objective optimal control problem that seeks to manage power flow in a power-split PHEV to minimize both health degradation and energy consumption cost. Third, we analyze the interplay between energy consumption cost and battery health degradation to understand the fundamental tradeoffs. The results of this research provide useful insight into health-conscious power management of lithium-ion battery storage systems.

The outline of this paper is as follows: Section 2 describes the model development, including the PHEV model, stochastic drive cycle model, and anode-side film growth model. Section 3 concisely summarizes the optimal control problem formulation. Section 4 presents and discusses the main results, including a tradeoff analysis of battery health and energy consumption cost. Finally, Section 5 summarizes the paper's main contributions and conclusions.

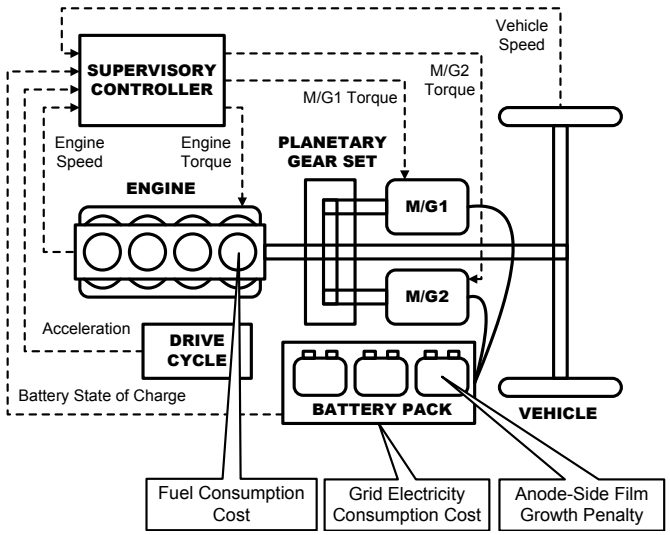

Figure 1. PHEV POWERTRAIN SYSTEM MODEL. THE SUPERVISORY CONTROLLER DETERMINES THE OPTIMAL ENGINE, M/G1, M/G2 TORQUE INPUTS AS A FUNCTION OF PHEV STATES TO MINIMIZE ENERGY CONSUMPTION AND BATTERY FILM GROWTH.

Table 1. GENERAL PHEV MODEL PARAMETERS

Vehicle	EPA Classification	Midsize Sedan
	HEV Configuration	Power-split
	Base Curb Weight	1471 kg
Engine	Type	Gasoline Inline 4-cylinder
	Displacement	1.5 L
	Max Power	57 kW @ 4500 RPM
	Max Torque	110 N-m @ 4500 RPM
Motor/ Generators	Type	Permanent Magnet AC
	M/G1 Max Power	30 kW @ 3000-5500 RPM
	M/G2 Max Power	35 kW @ 1040-5600 RPM
Battery Pack	Cell Chemistry	$LiFePO_4$
	Energy Capacity	5 kWh for pack
	Charge Capacity	2.3 Ah per cell
	Number of Cells	660

2 MODEL DEVELOPMENT

The PHEV modeled in this paper has a power-split configuration based upon THS-II [18], with a lithium-ion battery pack enlarged to a 5kWh energy capacity for plug-in operation [19]. General parameters for the vehicle are provided in Table 1. A schematic of the PHEV system, the supervisory controller, and

the relevant signals are given in Fig. 1. The state variables include engine speed, vehicle speed, battery state-of-charge (SOC) and acceleration. Acceleration is governed by a Markov chain which captures drive cycle dynamics, described in Section 2.2. We design this Markov chain to explicitly account for real-world daily trip length distributions - which is relevant for PHEVs that will potentially recharge overnight. In addition, we also include a battery health degradation model based upon an electrochemical anode-side film formation mechanism. In the following subsections we present descriptions and the governing equations for these models.

2.1 PHEV Model

2.1.1 Mechanical Subsystem The planetary gearset is at the heart of the power-split configuration. This three-port device couples the engine, motor/generator 1 (M/G1), and motor/generator 2 (M/G2) crankshafts. The dynamic-algebraic equations that describe this device are governed by Euler's law and a kinematic constraint relating component speeds [20]:

$$\begin{bmatrix} I_e & 0 & 0 & R+S \\ 0 & I_{M/G1} & 0 & -S \\ 0 & 0 & I'_{M/G2} & -R \\ R+S & -S & -R & 0 \end{bmatrix} \begin{bmatrix} \dot{\omega}_e \\ \dot{\omega}_{M/G1} \\ \dot{\omega}_{M/G2} \\ F_g \end{bmatrix} = \begin{bmatrix} T_e \\ T_{M/G1} \\ T'_{M/G2} \\ 0 \end{bmatrix} \quad (1)$$

The terms $I'_{M/G2}$ and $T'_{M/G2}$ are effective inertia and torques

$$I'_{M/G2} = I_{M/G2} + (I_w + mR_{tire}^2)/K^2 \quad (2)$$

$$T'_{M/G2} = T_{M/G2} + F_{road}R_{tire}/K \quad (3)$$

$$F_{road} = 0.5\rho C_d A_{fr} v^2 + \mu_{roll} mg \quad (4)$$

where F_{road} includes viscous aerodynamic drag and rolling friction forces.

Through algebraic matrix manipulations one may analytically solve for the state variables without explicitly determining the gear force F or inverting the matrix on the LHS of (1). This process results in two degrees of freedom, since there exist three ordinary differential equations and one algebraic constraint.

The control inputs include engine torque T_e and M/G1 torque $T_{M/G1}$. The engine is allowed to shut off by considering an "engine off" torque input command, which causes the engine speed to drop to zero within the span of one supervisory control time step (in this case 1 second). When positive torque is commanded from the engine while it is in the shutoff state, the engine is brought back to idle speed within one supervisory control time step. During both engine-on and engine-off modes, and transitions in between, the equations in (1)-(4) must be respected. For example, $\dot{\omega}_e = 0$ when the engine remains off. When the engine is commanded to turn on, then $\dot{\omega}_e$ must equal the appropriate value such that it reaches idle speed in the next simulation time step. M/G2 torque $T_{M/G2}$ is determined by the states and control inputs since $\dot{\omega}_{M/G2}$ is proportional to the acceleration state a according to $\dot{\omega}_{M/G2} = aK/R_{tire}$. Further details on the modeling of engine startup and shutdown will be reported in [21].

2.1.2 Electric Subsystem The battery pack is modeled by an equivalent circuit, which includes an open circuit voltage in series with an internal resistance. The parameters of this model have been identified experimentally on a custom-built hardware-in-the-loop setup, for commercial Li-ion cells containing $LiFePO_4$ cathode chemistries [22]. Both M/G1 and M/G2 interface with the battery pack, as shown in Fig. 1. These devices are modeled by power efficiency maps supplied by the Powertrain System Analysis Toolkit (PSAT) [23]. The electrical powertrain also consists of power electronics. However, their dynamics are ignored since they exceed the 1Hz bandwidth typically considered in power management studies. Hence, the governing equations for the electric subsystem are given by:

$$\dot{SOC} = -\frac{V_{oc} - \sqrt{V_{oc}^2 - 4P_{batt}R_{batt}}}{2Q_{batt}R_{batt}} \quad (5)$$

$$P_{batt} = T_{M/G1}\omega_{M/G1}\eta_{M/G1}^{k_{M/G1}} + T_{M/G2}\omega_{M/G2}\eta_{M/G2}^{k_{M/G2}} \quad (6)$$

$$k_i = \begin{cases} -1, & T_i\omega_i > 0 \\ 1, & T_i\omega_i \le 0 \end{cases} \quad \text{for} \quad i = \{M/G1, M/G2\} \quad (7)$$

To calculate the current I and voltage V_{cell} across each cell, one must know the battery pack configuration. That is, how many cells are arranged in series to produce the desired pack voltage, and how many parallel strings exist to achieve the desired energy capacity. Here we assume the use of 2.3 Ah 26650 format cells (to be consistent with our experimental batteries) arranged with $n_s = 110$ in series, and $n_p = 6$ parallel strings.

$$I = \dot{SOC} \cdot Q_{batt}/n_p \quad (8)$$

$$V_{cell} = (V_{oc} - IR_{batt})/n_s \quad (9)$$

Each cell is assumed to be identical or properly balanced through appropriate charge equalization schemes [24]. The current through each cell is used to calculate the anode-side film growth rate discussed in Section 2.3. The voltage calculation is used to ensure each cell does not exceed safe operating limits - which we implement mathematically as constraints in the problem formulation in Section 3.

2.2 Drive Cycle Model

An important new contribution we apply toward *plug-in* HEV power management is to model drive cycles with a first-order Markov chain *containing a terminal state*. Namely, the terminal state can represent "vehicle off" which signifies when the drive cycle terminates and no more cost accrues. This allows us to model distributions of drive cycle length directly.

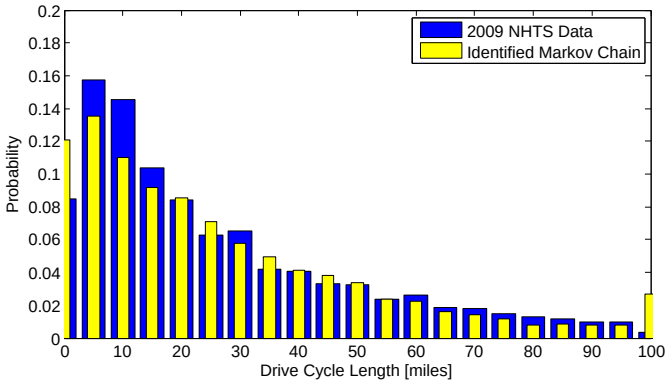

Figure 2. TRIP LENGTH DISTRIBUTION FOR 2009 NHTS DATA AND THE IDENTIFIED MARKOV CHAIN.

As demonstrated by O'Keefe and Markel [10], drive cycle length is critically important for *plug-in* HEV power management. They demonstrate that the optimal strategy rations battery charge through blending engine and battery power such that SOC reaches the minimum level exactly when the trip terminates, if the drive cycle is known *a priori*. This is in contrast to HEV power management, where battery SOC is typically sustained around a fixed value. This modeling approach is not new, and has been applied in the context of HEV power management [13]. Yet, its utility is particularly well suited for plug-in applications.

Mathematically, the Markov chain is given by

$$p_{ijm} = \Pr(a_{k+1} = j | a_k = i, v_k = m) \tag{10}$$
$$p_{itm} = \Pr(a_{k+1} = t | a_k = i, v_k = 0) \tag{11}$$
$$1 = \Pr(a_{k+1} = t | a_k = t, v_k = 0) \tag{12}$$

which maps acceleration-velocity pairs to a probability distribution over acceleration in the next time step (10)-(11). These transition probabilities are identified from certification cycles and real-world micro-trip data [1]. When acceleration reaches the terminal state t, it remains in that state with probability one (12).

Figure 2 demonstrates the distribution of trip length for the Markov chain, in which the transition probabilities p_{itm} in (11) have been identified from the 2009 National Household Travel Survey (NHTS) database [25]. Specifically, the probability of transition to "vehicle off" is zero unless the vehicle is completely stopped ($v_k = 0$) and has zero or small negative acceleration. Without adding distance as a state variable, it is difficult to perfectly match the Markov chain and NHTS data. Nevertheless this approach integrates a reasonably accurate representation of real-world trip lengths without adding an exponential increase in computational complexity - a key benefit.

In the main results presented in Section 4 we evaluate each controller across a library of 1,000 drive cycles generated from the Markov chain. This process enables us to quantify the performance metrics across a distribution of drive cycle characteristics, rather than single certification cycles such as FTP-72.

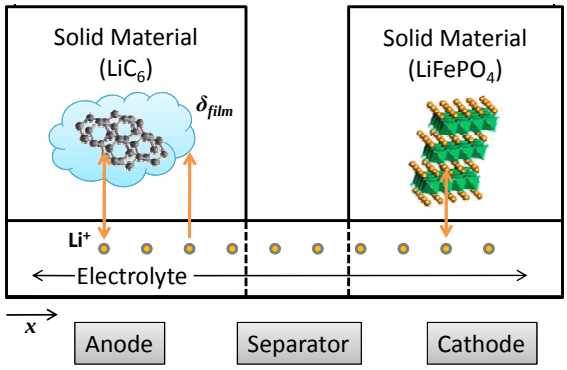

Figure 3. STRUCTURE OF THE ELECTROCHEMICAL LITHIUM-ION BATTERY CELL MODEL.

2.3 Anode-side Film Growth Model of Battery Aging

In this paper a function mapping cell state of charge (SOC) and current to film growth rate is extracted from an electrochemistry-based Li-ion battery cell model developed in [6]. This model simulates phenomena such as lithium ion diffusion and intercalation to determine the potential and concentration gradients in the solid and electrolyte sections of the anode, cathode, and separator. A schematic of the cell model is provided in Fig. 3, where Ramadass *et al.* argue that a resistive film builds up on the anode solid/electrolyte interface [6]. The exact chemical side reaction depends on the chemistry of the electrode and electrolyte. Equations (13)-(18), developed by Ramadass *et al.* argue that a simple and general method for modeling capacity loss is to assume an irreversible solvent reduction reaction of the following form

$$S + Li^+ + e^- \rightarrow P \tag{13}$$

where S denotes the solvent species and P is the product.

As a result of this irreversible side reaction, the products form a film at the solid/electrolyte interface, which has a time and spatially varying thickness $\delta_{film}(x,t)$ across the anode. This irreversibly formed film combines with the solid electrolyte interphase (SEI) resistance R_{SEI} to compose the total resistance at the solid/electrolyte interface as follows

$$R_{film}(x,t) = R_{SEI} + \frac{\delta_{film}(x,t)}{\kappa_P} \tag{14}$$

where κ_P, denotes the conductivity of the film, x is the spatial coordinate, and t is time. The state equation corresponding to the growth of film thickness, due to the unwanted solvent reduction described in (13), is given by

$$\frac{\partial \delta_{film}(x,t)}{\partial t} = -\frac{M_P}{a_n \rho_P F} J_s(x,t) \tag{15}$$

In (15), M_P, a_n, ρ_P, and F represent the product's molecular weight, specific surface area, mass density, and Faraday's constant, respectively. The term J_s denotes the local volumetric current density for the side reaction, which is governed by Butler-Volmer kinetics. If the solvent reduction reaction is irreversible and the variation of Li-ion concentration in the electrolyte is small, then we may approximate J_s by the Tafel equation [26].

$$J_s(x,t) = -i_{0,s} a_n e^{\left(\frac{-0.5F}{R_{gas}T}\eta_s(x,t)\right)} \tag{16}$$

In (16), $i_{0,s}$, R, and T respectively denote the exchange current density for the side reaction, universal gas constant, and cell temperature. The term η_s represents the side reaction overpotential, which drives the solvent reduction reaction in (13). The overpotential is calculated according to

$$\eta_s(x,t) = \phi_1(x,t) - \phi_2(x,t) - U_{s,ref} - \frac{J_{tot}(x,t)}{a_n} R_{film}(x,t) \tag{17}$$

The variables ϕ_1 and ϕ_2 represent solid and electrolyte potentials, respectively. The symbol $U_{s,ref}$ denotes the equilibrium potential of the solvent reduction reaction, which we assume to be constant. The total intercalation current J_{tot} represents the flow of charge exchanged with the anode-side electrolyte. Specifically, the total intercalation current J_{tot} is given by the sum of current between the solid and electrolyte (J_1), and the solvent reduction reaction and electrolyte (J_s), that is

$$J_{tot} = J_1 + J_s \tag{18}$$

Equations (14)-(18) encompass the film growth subsystem of the Li-ion battery cell model, adopted from [6]. This subsystem connects to the remainder of the battery model through the total intercalation current J_{tot} and potentials ϕ_1 and ϕ_2. Since these variables vary with respect to space (across the electrodes and separator) and time, they are determined by solving coupled partial differential-algebraic equations representing the concentration and potential distributions in the solid and electrolyte of the anode, cathode, and separator (see [4, 5] for details). Although this model captures complex physical phenomena such as coupled diffusion, intercalation, and film growth processes, its complexity makes control design for health management difficult. Therefore, the present research seeks to use the high fidelity model to generate simpler models for the purposes of control design. In the following, the anode-side film growth degradation dynamics will be approximated by a nonlinear static function, which enables optimal control design. Later work validates the control designs on the full electrochemical model.

To acquire insight on the relationship between battery cell SOC, current, and film growth rate, consider an ideal fresh cell, that is $\delta_{film}(x,0) = 0$. Suppose all the intercalation currents, overpotentials, and concentration profiles are constant with respect to space and correspond to zero initial applied current. Starting from these initial conditions, we simulate the electrochemical battery cell model for different initial SOC and applied current levels and measure the instantaneous film growth rate. From this data we produce a static relationship mapping cell SOC and applied current to the spatially averaged film growth rate $\dot{\bar{\delta}}_{film}$, shown in Fig. 4. The map indicates that film growth rate increases with cell SOC. The film growth rate also increases as the discharge current becomes increasingly negative, i.e. for increasing charge current. Finally, film grows when zero current is applied, indicating that aging occurs even when the cells are not in use - a fact previously reported in the literature [27] and commonly seen in practice.

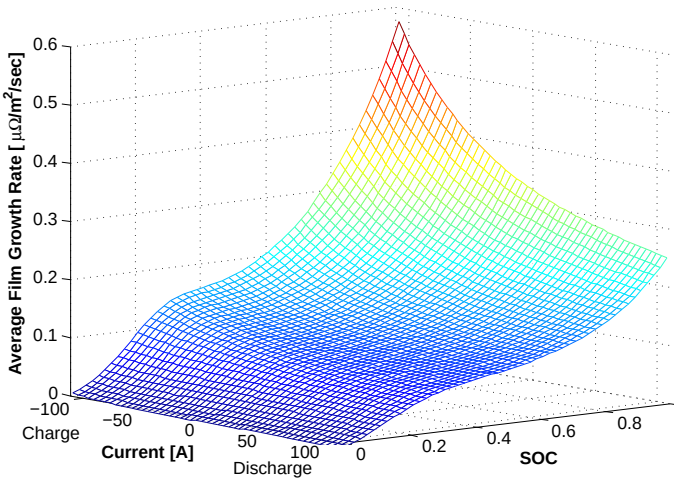

Figure 4. STATIC APPROXIMATION OF FILM GROWTH RATE VS. CELL CURRENT AND SOC UTILIZED FOR PHEV POWER MANAGEMENT CONTROL SYNTHESIS.

3 OPTIMAL CONTROL PROBLEM FORMULATION

The control objective is to synthesize a static function mapping the PHEV state variables to the engine and M/G1 torque inputs such that both energy consumption cost (i.e. fuel and grid electricity) and battery health degradation in terms of anode-side film growth are minimized. We formulate this as a shortest-path[1] stochastic dynamic programming problem.

$$\text{min:} \qquad J^g = \lim_{N\to\infty} \mathrm{E}\left[\sum_{k=0}^{N} c(x_k, u_k)\right] \tag{19}$$

$$\text{subject to:} \qquad x_{k+1} = f(x_k, u_k, w_k) \tag{20}$$

$$x \in X \tag{21}$$

$$u \in U(x) \tag{22}$$

[1]The shortest-path term [28] is used for Markov decision processes that contain a terminal state in the Markov chain, such as our drive cycle model.

where J^g is the cost for a given control policy g and $c(x_k, u_k)$ is a function that maps the state and control vectors to an instantaneous cost. The system dynamics summarized in discrete-time by (20) are provided in Section 2, with a one-second time step. This optimization is subject to sets of state and control constraints, X and $U(x)$ respectively, described in detail in Section 3.2. Our objective is to solve for the optimal control policy g^* which satisfies.

$$g^* = \arg \inf_{g \in \mathcal{G}} J^g \tag{23}$$

where $\mathcal{G}$ denotes the set of all feasible control policies.

3.1 Objective Function

The minimization of both energy consumption cost and battery health is, generally speaking, a multi-objective optimal control problem. For simplicity, we combine both objectives into a scalar objective with linear weighting α, given mathematically by

$$c(x_k, u_k) = \alpha \cdot c_{energy}(x_k, u_k) + (1-\alpha) \cdot c_{film}(x_k, u_k) \tag{24}$$

where the individual objective functions are given by

$$c_{energy}(x_k, u_k) = \beta \alpha_{fuel} W_{fuel} + \alpha_{elec} \frac{-V_{oc} Q_{batt} S\dot{O}C}{\eta_{grid}} \tag{25}$$

$$c_{film}(x_k, u_k) = \dot{\delta}_{film}(I, SOC) \tag{26}$$

Equation (25) represents the instantaneous energy consumption cost in USD, which includes both fuel and grid charging costs - weighted according to the energy price ratio β (see [1] for more details). Throughout this paper, we use $\beta = 0.8$, consistent with the average energy prices in June 2010, namely \$2.73 USD per gallon of gasoline [29] and \$0.094 USD per kWh of electricity [30]. Equation (26) represents the instantaneous anode-side film growth in a single battery cell, characterized by the map depicted in Fig. 4. Additionally, both objectives are normalized by scaling the range of their natural values to values between zero and one.

We vary the weighting α in (24) between zero and one to obtain the convex subset of the Pareto optimal control policies. Future work may apply multi-objective dynamic programming techniques to acquire the entire Pareto optimal set [31]. Henceforth, we refer to the convex subset of Pareto optimal solutions as, simply, the Pareto set - although this is admittedly an abuse of terminology.

3.2 Constraints

In addition to minimizing the aforementioned objectives, the power management algorithm satisfies constraints on both the states and control actions. These constraints correspond to physical operating limits, zones of safe operation, and actuation limits. Rate of change constraints are not considered here, although they can be easily added in this formulation. The state constraints are given by

$$\omega_{e,min}(T_e) <= \omega_e <= \omega_{e,max} \tag{27}$$

$$\omega_{M/G1,min} <= \omega_{M/G1} <= \omega_{M/G1,max} \tag{28}$$

$$\omega_{M/G2,min} <= \omega_{M/G2} <= \omega_{M/G2,max} \tag{29}$$

$$SOC_{min} <= SOC <= SOC_{max} \tag{30}$$

Minimum engine speed is equal to idle speed when the engine is on, which is typically enforced for combustion stability, noise, vibration, and harshness. Minimum engine speed is zero otherwise. The minimum M/G1 speed constraint also produces an interesting effect in a power-split configuration. If the engine is off, then $\omega_{M/G1}$ will violate its minimum value if vehicle speed, which is proportional to $\omega_{M/G2}$, is sufficiently high, due to the kinematic relationship in (1). Consequently the engine must turn on for vehicle speeds greater than 36 mph, even when sufficient battery charge exists to run in all-electric mode.

The control constraints are given by the following:

$$T_{e,min} <= T_e <= T_{e,max}(\omega_e) \tag{31}$$

$$T_{M/G1,min} <= T_{M/G1} <= T_{M/G1,max} \tag{32}$$

$$T_{M/G2,min} <= T_{M/G2} <= T_{M/G2,max} \tag{33}$$

$$V_{cell,min} <= V_{cell} <= V_{cell,max} \tag{34}$$

The minimum M/G2 torque is determined by two constraints: saturation limits on M/G2 and the maximum battery pack voltage, which can be violated if too much regenerative power is supplied to the battery at, for example, high SOC levels. Hence the minimum M/G2 torque is a function of several states and control inputs $T_{M/G2,min} = T_{M/G2,min}(SOC, \omega_{M/G1}, T_{M/G1}, \omega_{M/G2})$. The residual M/G2 torque after applying these constraints is provided by hydraulic braking.

To enforce both the state and control constraints we apply the following method. For all state and control pairs we simulate the subsequent state using (20). If any constraints are violated then the corresponding control inputs are removed from the set of admissible controls, for the given state. This process generates the set of admissible controls $U(x)$ for each state, which can be computed offline from the stochastic dynamic programming algorithm.

Numerically, this problem is solved via modified policy iteration, where the policy evaluation step is approximated through successive value iterations. This algorithm has the property that convergence to the optimal policy occurs in finite time [28]. Since we solve the stochastic dynamic programming problem for a sweeping range of α, and simulate the resulting controllers

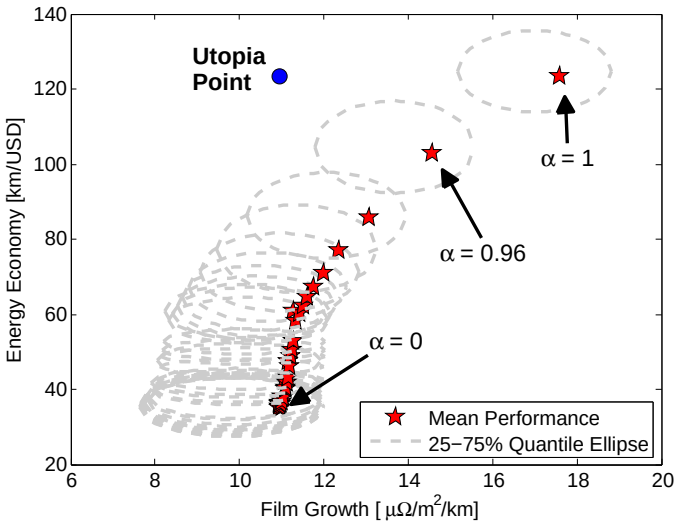

Figure 5. PARETO SET OF OPTIMAL CONTROLLERS FOR ANODE-SIDE FILM GROWTH AND ENERGY ECONOMY, SIMULATED ACROSS A LIBRARY OF 1,000 RANDOMLY GENERATED DRIVE CYCLES. STARS ($\star$) INDICATE THE AVERAGE VALUES AND THE DASHED LINES (- -) ARE THE 25/75% QUANTILE RANGE.

across 1,000 cycles each, we leverage parallel computing resources at the University of Michigan Center for Advanced Computing.

4 MAIN RESULTS

This section examines the performance of supervisory control algorithms that optimally tradeoff battery aging with energy consumption cost. To obtain a measure of controller performance across a variety of drive cycle behavior (as opposed to single certification cycles), we apply the following procedure:

1. The Pareto optimal set of controllers is synthesized via the stochastic dynamic program formulated in Section 3.
2. A library of 1,000 drive cycles is generated from the Markov chain described in Section 2.2.
3. Each controller in the Pareto set is simulated for all drive cycles in the library.
4. Performance characteristics, including film growth and energy cost, are recorded.

Subsequently, we analyze three controllers of interest from the Pareto set on single certification cycles to obtain a fundamental understanding of how to optimally tradeoff battery health and energy consumption through proper SOC management.

4.1 Energy Consumption vs. Film Growth

Performance results for the Pareto set of controllers that optimally tradeoff film growth (per battery cell) with energy consumption costs are presented in Fig. 5. This is achieved by

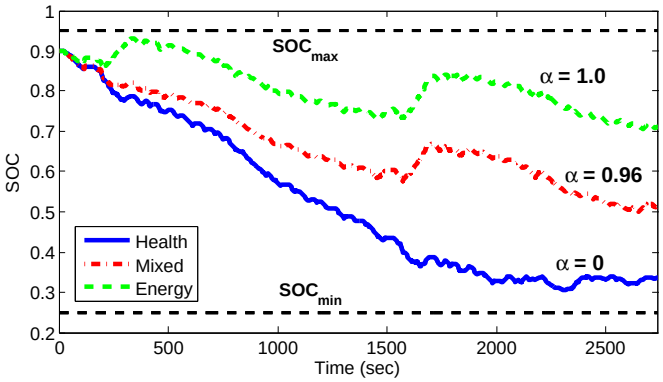

Figure 6. SOC TRAJECTORIES FOR HEALTH ($\alpha = 0$), MIXED ($\alpha = 0.96$), AND ENERGY ($\alpha = 1.0$) OPTIMAL CONTROLLERS ON TWO CONCATENATED FTP-72 CYCLES.

sweeping the weighting parameter α in (24) from zero to one. A distribution of performance metrics is obtained for simulating the controllers across the entire library of drive cycles. As such, Fig. 5 indicates the average values as well as the 25/75% quantile ranges. The horizontal axis reports the film growth resistance per km, while the vertical axis indicates energy economy in km/USD (analogous to miles per gallon). The utopia point is located in the upper-left, which indicates the individually achievable optimal performance metrics.

This plot indicates that, indeed, there exists a fundamental tradeoff between anode-side film growth in battery packs and energy consumption costs. Namely, average film growth can be reduced by 37% relative to an "energy-only" controller, but at the sacrifice of a 70% decrease in average energy economy. The reason the distributions of film growth stretch left of the mean is related to the distribution of trip length. As trips become longer, more battery SOC is depleted and film growth rate decreases. Normalizing this effect against longer distances traveled produces a long tail toward the left side of Fig. 5.

4.2 Optimal Solution Analysis

To acquire physical insight into the structural properties of the optimal controllers, we analyze three solutions from the Pareto set, $\alpha = 1.0, 0.96$, and 0. Generally speaking these respectively correspond to emphasizing energy only, energy mostly and a little health, and health only. The controller corresponding to $\alpha = 0.96$ is chosen because it represents the best balance between both objectives, measured in terms of the normalized 2-norm distance from the utopia point in Fig. 5. These controllers are simulated on two concatenated FTP-72 cycles.

Figure 6 demonstrates the SOC trajectories for each controller. The energy-only controller ($\alpha = 1.0$) conservatively rations battery charge by blending engine and battery power. This process reduces the time spent in charge sustenance mode, where fuel must be consumed to meet power demand and sustain battery charge [1]. Put simply, charge sustenance mode is extremely

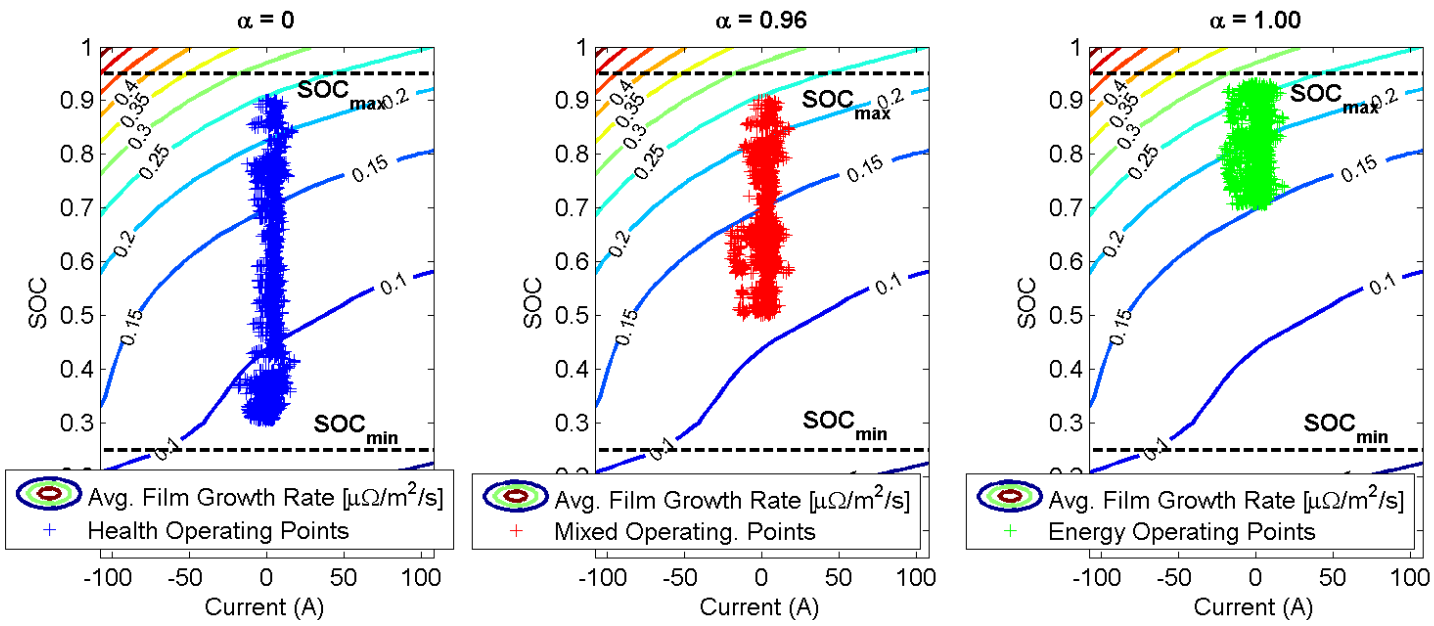

Figure 7. OPERATING POINTS ON ANODE-SIDE FILM GROWTH RATE MAP FOR HEALTH ($\alpha = 0$), MIXED ($\alpha = 0.96$), AND ENERGY ($\alpha = 1.0$) OPTIMAL CONTROLLERS ON TWO CONCATENATED FTP-72 CYCLES.

expensive relative to charge depletion, and should be avoided, if possible, to reduce energy consumption cost. If the drive cycle were known beforehand, the optimal strategy would blend engine and battery power so battery SOC reaches its minimum level exactly when the trip terminates. Recall that trip length distributions are directly implemented into the problem formulation through the terminal state of the Markov chain, as described in Section 2.2. Hence the controller is trip length-conscious. In contrast, the health-only controller ($\alpha = 0$) aggressively depletes battery charge to avoid the high film growth rates seen in Fig. 4. This results in a strategy that mimics electric-only operation, followed by charge sustenance. Interestingly, the mixed ($\alpha = 0.96$) controller's characteristics are more similar to $\alpha = 0$ than $\alpha = 1$. The reason can be understood by analyzing the gradient properties of the film growth map. Namely, the steep gradient at high SOC values indicates significant benefits in accumulated film growth can be achieved by quickly depleting charge. This is in spite of heavily weighting energy costs over battery health, since instantaneous energy cost as defined in (25) is relatively insensitive to SOC. Conversely, film growth is very sensitive to SOC. Mathematically this is shown from (25)-(26)

$$\frac{\partial c_{film}}{\partial SOC} \gg \frac{\partial c_{energy}}{\partial SOC} \tag{35}$$

$$\Leftrightarrow \frac{\partial \dot{\delta}_{film}(I,SOC)}{\partial SOC} \gg -\alpha_{elec}\frac{Q_{batt}\dot{SOC}}{\eta_{grid}}\frac{dV_{oc}(SOC)}{dSOC} \approx 0 \tag{36}$$

where the RHS of (36) is approximately zero because a typical Li-ion battery has nearly constant open-circuit voltage with respect to SOC, in the allowable SOC range.

This result is clearly illustrated in Fig. 7, which indicates the operating points of each controller superimposed on the film growth map from Fig. 4. Observe that adding a small consideration for battery health (e.g. $\alpha = 0.96$) to an energy-only objective (e.g. $\alpha = 1.0$) dramatically changes the operating point behavior. Namely, it induces the controller to escape high film growth rate regions by depleting battery charge quickly until it reaches a lower SOC level (between 50-60%). However, it leaves enough available battery energy to blend power until the trip ends, without entering charge sustenance (near 25% SOC). In summary, a PHEV power management strategy that considers film growth in addition to energy consumption will, in general: (1) deplete battery charge quickly to reduce film growth rates, then (2) blend engine and battery power to avoid charge sustenance.

In this study we focus on one particular battery degradation mechanism - anode-side film growth. In truth a myriad of mechanisms exist that cause capacity fade in lithium-ion batteries, although film growth has been identified as one of the most significant [3]. A comprehensive review of these mechanisms can be found in [3] and the references therein. From a systems-level perspective degradation can be associated with SOC, temperature, depth of discharge, cycling, etc. Experiments identifying several of these relationships are currently underway in our laboratory. Nonetheless the application of an established degradation model [6] represents a reasonable first step toward health-conscious power management.

5 CONCLUSIONS

This paper examines health-conscious power management in plug-in hybrid electric vehicles through electrochemical modeling and stochastic control. Namely, we formulate a multi-objective optimal control problem which optimally trades off battery health in terms of anode-side resistive film formation with energy consumption cost (fuel and grid electricity). The problem formulation includes a reduced form of a degrading electrochemical battery model from the literature [6]. In addition, we apply a shortest path stochastic dynamic programming formulation. This enables us to match the Markov chain drive cycle model with real-world daily trip length distributions reported by the National Household Travel Survey [25].

Analysis of the optimal power management algorithms indicates that an energy-focused controller *conservatively* depletes SOC by blending engine and battery power. This reduces the time spent in charge sustenance mode, where relatively expensive fuel is required to meet driver power demand and sustain battery charge. A health-focused controller *aggressively* depletes SOC, since the anode-side film grows faster at high SOC levels. A controller which considers both objectives will aggressively deplete SOC first, to reduce film growth rates, then conservatively blend engine and battery power to limit entry into charge sustenance mode.

ACKNOWLEDGMENT

This research is financially supported by the National Science Foundation Graduate Research Fellowship Program.

REFERENCES

[1] Moura, S. J., Fathy, H. K., Callaway, D. S., and Stein, J. L., 2010. "A Stochastic Optimal Control Approach for Power Management in Plug-in Hybrid Electric Vehicles". *accepted to IEEE Trans. on Control Systems Technology*.

[2] Moura, S. J., Forman, J. C., Stein, J. L., and Fathy, H. K., 2009. "Control of Film Growth in Lithium Ion Battery Packs via Switches". *2009 ASME Dynamic Systems and Control Conference*.

[3] Aurbach, D., 2000. "Review of selected electrode-solution interactions which determine the performance of Li and Li ion batteries". *J. of Power Sources,* **89**(2), pp. 206 – 18.

[4] Doyle, M., Fuller, T., and Newman, J., 1993. "Modeling of galvanostatic charge and discharge of the lithium/polymer/insertion cell". *Journal of the Electrochemical Society,* **140**(6), pp. 1526 – 33.

[5] Fuller, T., Doyle, M., and Newman, J., 1994. "Simulation and optimization of the dual lithium ion insertion cell". *Journal of the Electrochemical Society,* **141**(1), pp. 1 – 10.

[6] Ramadass, P., Haran, B., Gomadam, P., White, R., and Popov, B., 2004. "Development of first principles capacity fade model for Li-ion cells". *Journal of the Electrochemical Society,* **151**(2), pp. 196 – 203.

[7] Musardo, C., Rizzoni, G., Guezennec, Y., and Staccia, B., 2005. "A-ECMS: An adaptive algorithm for hybrid electric vehicle energy management". *European Journal of Control,* **11**(4-5), pp. 509–524.

[8] Vahidi, A., Stefanopoulou, A., and Peng, H., 2006. "Current management in a hybrid fuel cell power system: A model-predictive control approach". *IEEE Transactions on Control Systems Technology,* **14**(6), pp. 1047–1057.

[9] Gong, Q., Li, Y., and Peng, Z.-R., 2008. "Trip-based optimal power management of plug-in hybrid electric vehicles". *IEEE Transactions on Vehicular Technology,* **57**(6), pp. 3393–3401.

[10] O'Keefe, M. P., and Markel, T., 2006. "Dynamic Programming Applied to Investigate Energy Management Strategies for a Plug-In HEV". *22nd International Battery, Hybrid and Fuel Cell Electric Vehicle Symposium, (EVS-22)*, October 23, 2006.

[11] Lin, C.-C., 2004. "Modeling and Control Strategy Development for Hybrid Vehicles". PhD thesis, University of Michigan, Ann Arbor.

[12] Kum, D., Peng, H., and Bucknor, N. "Modeling and control of hybrid electric vehicles for fuel and emission reduction". In 2008 ASME Dynamic Systems and Control Conference, pp. 1247–1254.

[13] Opila, D. F., Aswani, D., McGee, R., Cook, J. A., and Grizzle, J. W., 2008. "Incorporating drivability metrics into optimal energy management strategies for hybrid vehicles". *47th IEEE Conference on Decision and Control*, pp. 4382–9.

[14] Amiri, M., Esfahanian, M., Hairi-Yazdi, M. R., and Esfahanian, V., 2009. "Minimization of power losses in hybrid electric vehicles in view of the prolonging of battery life". *Journal of Power Sources,* **190**(2), pp. 372 – 379.

[15] Shidore, N., Kwon, J., and Vyas, A., 2009. "Trade-off between PHEV fuel efficiency and estimated battery cycle life with cost analysis". *5th IEEE Vehicle Power and Propulsion Conference*, pp. 669 – 677.

[16] Amjadi, Z., and Williamson, S. S., 2010. "Power-electronics-based solutions for plug-in hybrid electric vehicle energy storage and management systems". *IEEE Transactions on Industrial Electronics,* **57**(2), pp. 608 – 616.

[17] Mi, C., Li, B., Buck, D., and Ota, N., 2007. "Advanced electro-thermal modeling of lithium-ion battery system for hybrid electric vehicle applications". *2007 IEEE Vehicle Power and Propulsion Conference*, pp. 107 – 111.

[18] Muta, K., Yamazaki, M., and Tokieda, J., 2004. "Development of New-Generation Hybrid System THS II - Drastic Improvement of Power Performance and Fuel Economy". *2004 SAE World Congress, SAE Paper 2004-01-0064*.

[19] English, A., 2009. "2012 Toyota Plug-in Prius Review". *Popular Mechanics*.

[20] Liu, J., 2007. "Modeling, Configuration and Control Optimization of Power-Split Hybrid Vehicles". PhD thesis, University of Michigan, Ann Arbor.

[21] Moura, S. J., 2011. "Optimal Control of Energy Systems

for Lithium-ion Battery Health". PhD thesis, in progress, University of Michigan, Ann Arbor.

[22] A123 SYSTEMS, 2006. *High Power Lithium Ion ANR26650M1 Data Sheet*.

[23] Rousseau, A., Kwon, J., Sharer, P., and Duoba, M., 2006. "Integrating Data, Performing Quality Assurance, and Validating the Vehicle Model for the 2004 Prius Using PSAT". *SAE Papers 2006-01-0667*.

[24] Baughman, A., and Ferdowsi, M., 2005. "Battery charge equalization-state of the art and future trends". *SAE Transactions: Electronic and electrical systems, Paper No. 2005-01-3474*.

[25] USDOT-FHWA, 2009. National Household Travel Survey. Tech. rep., U.S. Department of Transportation, Federal Highway Administration. http://nhts.ornl.gov/index.shtml.

[26] Newman, J., 1991. *Electrochemical Systems*, 2nd ed. Prentice Hall.

[27] Broussely, M., Biensan, P., Bonhomme, F., Blanchard, P., Herreyre, S., Nechev, K., and Staniewicz, R., 2005. "Main aging mechanisms in Li ion batteries". *Journal of Power Sources,* **146**(1-2), pp. 90 – 96.

[28] Bertsekas, D., 2005. *Dynamic Programming and Optimal Control, Vols I and II*. Athena Scientific.

[29] AAA, 2010. Daily fuel gauge report. Tech. rep., AAA. http://www.fuelgaugereport.com/.

[30] US-DOE, 2010. Average retail price of electricity to ultimate customers by end-use sector, by state. Tech. rep., U.S. Energy Information Administration. http://www.eia.doe.gov/electricity/epm/table5_6_b.html.

[31] Wiering, M. A., and De Jong, E. D., 2007. "Computing optimal stationary policies for multi-objective markov decision processes". *Proceedings of the 2007 IEEE Symposium on Approximate Dynamic Programming and Reinforcement Learning, ADPRL 2007*, pp. 158 – 165.

Appendix A: Nomenclature

Symbol	Description	Units
A_{fr}	Effective frontal area of vehicle	[m^2]
a	Vehicle acceleration	[m/s^2]
a_n	Specific surface area of anode	[m^2/m^3]
C_d	Aerodynamic drag coefficient	[-]
$c(\cdot,\cdot)$	Instantaneous cost function	
F	Faraday's constant	[C/mol]
F_g	Planetary gear force	[N]
I	Current through each cell	[A]
I_e	Engine inertia	[kg·m^2]
$I_{M/G1}$	Motor/generator 1 inertia	[kg·m^2]
$I_{M/G2}$	Motor/generator 2 inertia	[kg·m^2]
I_w	Wheel inertia	[kg·m^2]
i_0	Battery pack current	[A]
$i_{0,s}$	Exchange current density for side reaction	[A/m^2]
i_1, i_2	Cell current	[A]
J^g	Optimal cost for control policy g	[-]
J_s	Current density of side reaction	[A/m^3]
K	Final drive ratio	[-]
M_P	Molecular weight of product from side reaction	[mol/kg]
m	Vehicle mass	[kg]
n_p	Number of parallel strings of cells	[-]
n_s	Number of cells in series per string	[-]
P_{batt}	Power transfer from battery pack	[W]
Q_{batt}	Battery pack charge capacity	[A·s]
R	Number of teeth on ring gear	[-]
R_{gas}	Universal gas constant	[J/K/mol]
R_{batt}	Internal resistance of battery pack	[Ω]
R_{SEI}	Resistance of solid electrolyte interphase (SEI)	[Ω/m^2]
R_{tire}	Tire radius	[m]
S	Number of teeth on sun gear	[-]
SOC	Battery state of charge	[-]
T_e	Engine torque	[N·m]
$T_{M/G1}$	Motor/generator 1 torque	[N·m]
$T_{M/G2}$	Motor/generator 2 torque	[N·m]
$U_{s,ref}$	Equilibrium potential of side reaction	[V]
$U(x)$	Admissible set of controls	
V_{cell}	Voltage of individual battery cell	[V]
V_{oc}	Battery pack open circuit voltage	[V]
v	Vehicle speed	[m/s]
W_{fuel}	Mass flow rate of fuel	[g/s]
X	Admissible set of states	
x	Spatial coordinate across cell	[m/m]
α	Linear objective weight	[-]
β	Energy price ratio	[USD/USD]
$\overline{(\delta_{film})}$	(Spatially averaged) anode-side resistive film thickness	[pm/m^2]
δ_{film}		
η_{grid}	Grid-to-PHEV charging efficiency	[-]
$\eta_{M/G1}$	Motor/generator 1 power efficiency	[-]
$\eta_{M/G2}$	Motor/generator 2 power efficiency	[-]
η_s	Over potential driving side reaction	[V]
κ_P	Conductivity of electrolyte	[1/m/Ω]
μ_{roll}	Rolling friction coefficient	[-]
ρ	Air density	[kg/m^3]
ρ_P	Side reaction product density	[kg/m^2]
ϕ_1, ϕ_2	Solid, electrolyte potential	[V]
ω_e	Engine crankshaft speed	[rad/s]
$\omega_{M/G1}$	Motor/generator 1 speed	[rad/s]
$\omega_{M/G2}$	Motor/generator 2 speed	[rad/s]